Electrochimica Acta 302 (2019) 71–77

Contents lists available at ScienceDirect

Electrochimica Acta

journal homepage: www.elsevier.com/locate/electacta

Quantitative characterization of a voltage-dependent pseudocapacitance on heteroatom-enriched nanoporous carbons

Jae Kyeong Han [a, 1], Min Eui Lee [a, 1], Hyoung Jin Choi [a], Hyoung-Joon Jin [a, **], Young Soo Yun [b, *]

[a] Department of Polymer Science and Engineering, Inha University, Incheon 22212 South Korea
[b] Department of Chemical Engineering, Kangwon National University, Samcheok 25913 South Korea

ARTICLE INFO

Article history:
Received 23 November 2018
Received in revised form
17 January 2019
Accepted 3 February 2019
Available online 8 February 2019

Keywords:
Pseudocapacitance
Nanoporous carbon
Electrode
Supercapacitor
Ion batteries

ABSTRACT

Nanostructured carbons with a number of redox-active sites play a key role as active electrode materials for supercapacitors and rechargeable batteries, owing to their pseudocapacitive charge storage behaviors. Nevertheless, there is currently no method to characterize the level of contribution of pseudocapacitance in overall capacitance values, hindering technological and scientific advancement of pseudocapacitive electrode materials. In this study, we can observe the voltage-dependent pseudocapacitive behaviors of heteroatom-enriched nanoporous carbons, which can be detected through a simple comparison of electrochemically obtained results in both aqueous and organic electrolyte systems. It is also confirmed that the voltage-dependent pseudocapacitive behaviors are so fast and stable that the heteroatom-enriched nanoporous carbons based on the voltage-dependent pseudocapacitive behaviors can deliver high specific energy and power as cathodes when they are assembled with a proper counterpart anode.

1. Introduction

A pseudocapacitive reaction (PCR) is a surface and/or near surface charge storage behavior accompanying a charge transfer between a guest ion and host active material [1–3]. The surface-induced charge transfer reaction is very fast and stable, because it occurs without solid-state-diffusion of the guest ion and volume changes in the active materials [4–7]. In addition, a large amount of charge surpassing that gathered from electrochemical double layer (EDL) formation can be stored by PCRs [7–12]. The more compelling characteristic of the PCR is its collaborative charge storage phenomenon coinciding with EDLs. When the PCR occurs on nanoporous carbon (NPC)-based electrode materials, a drastic improvement in capacity can be achieved with preservation of their intrinsic characteristics that arise from the storage nature of the surface-driven charge [7,10,13–16]. Several reports have demonstrated the superiority of NPCs with PCRs, detailing their significantly high electrochemical performances as active electrode materials for Li and Na ion batteries as well as supercapacitors [13–18]. Nevertheless, there is little information for the chemisorption-based alkali cation storage behaviors on NPCs. Moreover, there is no method to characterize the level of contribution of the PCR and EDL capacitance, limiting deeper understanding of the PCR in NPCs. Herein, we focused on that the PCRs on NPCs occur through various reaction pathways which have intrinsic activation energy barriers. Therefore, voltage hysteresis of their electrochemical charge/discharge profiles is inevitable in a given voltage window. Owing to the voltage hysteresis, the charge storage capacitance is dependent on the operating voltage window, which could results in variation in the capacitance value according to the characterized voltage range. The voltage-dependent pseudocapacitive behaviors (VD-PCBs) may be used to differentiate the respective contributions of the EDL capacitance and PCR to the overall capacity of NPCs.

In this study, heteroatom-enriched NPCs (H–NPCs) were prepared from a nitrogen-containing conjugated polymer precursor by pyrolysis with potassium hydroxide. The voltage-dependent charge storage behaviors of H–NPCs were then characterized by cyclic voltammetry (CV) in different electrolyte systems. From the results, it was confirmed that the pseudocapacitance value can be

* Corresponding author.
** Corresponding author.
E-mail addresses: hjjin@inha.ac.kr (H.-J. Jin), ysyun@kangwon.ac.kr (Y.S. Yun).
[1] These authors contributed equally to this work.

https://doi.org/10.1016/j.electacta.2019.02.009
0013-4686/

quantitatively measured through a comparison of CV obtained from different charge carriers. The VD-PCBs on H–NPCs were kinetically fast and highly stable, leading to a high electrochemical performance. In addition, H–NPCs-based lithium ion hybrid capacitors achieved a high specific energy of ~220 Wh kg^{-1} and a specific power of ~5400 W kg^{-1} with a long-term cycle life of over 500 cycles, demonstrating the usefulness of the VD-PCBs-based H–NPCs.

2. Experimental

Preparation of H–NPCs and highly reduced H–NPCs (RH-NPCs): H–NPCs were prepared from polypyrrole nanotubes (PNTs) by pyrolysis with potassium hydroxide (PNT:KOH of 1:1 w/w). The PNTs were synthesized by using a reactive self-degraded template [19]. Briefly, 0.7 mL of pyrrole was added to 200 mL of a 5 mM methyl orange aqueous solution at a thermostat condition of 5 °C. 10 mmol of iron (III) chloride hexahydrate was dissolved in 23 mL of deionized water and added drop-wise for 2 h. The mixtures were then gently stirred for 24 h. The resulting polypyrrole precipitate was separated by filtration and purified by Soxhlet extraction using acetone until the extracts were colorless. Then, the product, PNT, was washed with ethanol and dried at 40 °C in a vacuum oven. The pyrolysis process was conducted using a tube furnace at 800 °C for 2 h. A heating rate of 5 °C min^{-1} and nitrogen flow of 200 mL min^{-1} were applied for the process. RH-NPCs were prepared by heating H–NPCs at 800 °C under a mixed Ar/H_2 (4 wt%) flow at 200 mL min^{-1}.

Characterization: The morphologies and microstructures of H–NPCs and RH-NPCs were examined by field emission-scanning electron microscopy (FE-SEM, S-4300, Hitachi, Japan) and high-resolution transmission electron microscopy (HR-TEM, JEM-ARM-200F, JEOL, Japan). X-ray diffraction (XRD, Rigaku, DMAX 2500) analysis was performed using Cu-K_α radiation ($\lambda = 0.154$ nm) generated at 40 kV and 100 mA. Raman spectra were recorded using a continuous-wave linearly polarized laser (514.5 nm, 2.41 eV, 16 mW). The laser beam was focused using a 100 × objective lens, resulting in a spot with a 1-μm diameter. The acquisition time and number of cycles for the collection of each spectrum were 10 s and 3, respectively. The chemical compositions of the samples were determined by X-ray photoelectron spectroscopy (XPS, PHI 5700 ESCA, USA) using monochromatic Al K_α radiation ($h\nu = 1486.6$ eV). The pore structures of H–NPCs and RH-NPCs were characterized by nitrogen adsorption/desorption isotherms that were analyzed using a surface area and porosimetry analyzer (ASAP 2020, Micromeritics, USA) at −196 °C.

Electrochemical characterization: The electrochemical performances of H–NPCs and RH-NPCs were characterized using a device (Autolab PGSTAT302N, Switzerland, Metrohm AG) and the Wonatec automatic battery cycler with CR2032-type coin cells. Aqueous electrolytes were prepared by dissolving 2 M LiOH, 2 M NaOH, 2 M KOH, 0.5 M Li_2SO_4, 0.5 M Na_2SO_4, or 0.5 M K_2SO_4 in distilled water. The half-cell tests in the aqueous electrolytes were performed by a beaker cell with a three-electrode configuration. SHE and Pt electrodes were used as reference and counter electrodes, respectively. Furthermore, an organic electrolyte was prepared by dissolving 1 M $LiPF_6$ (Sigma-Aldrich, USA, purity: 99.9%) in a mixture of ethylene carbonate and dimethyl carbonate (1:1 v/v). A glass microfiber filter (GF/F, Whatman) was used as a separator. The working electrode was made by mixing the active material (90 wt%) and polyvinylidene fluoride (10 wt%) in N-methyl-2-pyrrolidone. The as-obtained slurries were homogeneously coated on Cu and Al foil, which served as the anode and cathode, respectively. Discs with a diameter of 0.5″, which served as the electrodes for the cells, were punched out of the coated foil sheets, and mass-loading of active materials was ~2 mg cm^{-2}. Lithium metal was used as the reference and counter electrode for the half cell tests. Full cells were assembled after pre-cycling of the respective electrode materials in the half cell configuration for 10 cycles. In the pre-cycling process of the nano-graphite//H–NPCs cell, the anode and cathode voltages were tuned to 1.5 V vs. Li^+/Li by charge injection. The H-NPC cathode was operated from 1.5 to 4.5 V, and the nano-graphite anode from 0.01 to 1.5 V. In contrast, the H–NPCs//H–NPCs cell was tested without charge injection after pre-cycling.

3. Results and discussion

PNTs with diameters of approximately 30–50 nm as shown in Fig. S1 were heated with potassium hydroxide at 800 °C under an Ar atmosphere to prepare H–NPCs possessing a large number of redox-active heteroatoms and nanopores. After the chemical activation process, the initial morphologies of the PNTs were fully collapsed, and random shaped particles with frayed surfaces were observed in a FE-SEM image (Fig. 1(a)). In addition, HR-TEM images indicated that H–NPCs have highly disordered carbon structures with a poor graphitic ordering (Fig. 1(b)). The amorphous carbon structure is induced by chemical activation of potassium hydroxide, which occurs in two steps [20]. The first activation is caused by oxidation of the carbon structure and followed by the emission of CO and CO_2 gases with the catalytic assistance of alkali metals. The next activation process occurs when metallic potassium is formed at temperatures above 700 °C. The metallic potassium penetrates the graphitic lattice formed during pyrolysis, resulting in a highly disordered carbon structure with a worn-out surface. Raman spectra and XRD patterns provide further detailed information about the microstructure of the H–NPCs (Fig. 1(c–e)). The Raman spectrum shows broad *D* and *G* band peaks at ~1343 and ~1575 cm^{-1}, respectively (Fig. 1(c)). The *D* band originates from the intrinsic phonon mode with A_{1g} symmetry of the infinite poly-aromatic carbon ring that is activated by the structural disorder [21]. In contrast, the *G* band represents the poly-hexagon carbon structure related to the E_{2g} vibration mode of the *sp* [2]-hybridised carbon atoms [21]. From the presence of *D* and *G* bands, it can be confirmed that H–NPCs are composed of poly-hexagonal carbon building blocks including defective carbon structures. The *D* to *G* band intensity ratio (I_D/I_G) indicates the domain size (L_a) of the ordered poly-aromatic $I_D/I_G = C(\lambda)/L_a$ hexagonal carbon ring structure, which can be calculated by a simple equation:, where $C(\lambda)$ is a constant that depends on the laser wavelength ($C(\lambda) = 4.4$ nm for a the 514 nm laser used here) [21]. The I_D/I_G value of the H–NPCs is 1.02, corresponding to a domain size of ~4.4 nm. The XRD patterns also support the finding that H–NPCs are composed of defective poly-hexagonal carbon building blocks. The pattern shows a broad graphite (002) peak at 23°, indicating poor stacking ordering (Fig. 1(e)). To compare the effects of heteroatoms in PCR, RH-NPCs were also prepared by thermal treatment of H–NPCs under a hydrogen gas atmosphere. It was confirmed that the thermal reduction process insignificantly affects the microstructure of RH-NPCs as their Raman spectra and XRD patterns are similar to those of H–NPCs, as shown in Fig. 1(d) and (e).

The porous properties of H–NPCs and RH-NPCs were characterized by nitrogen adsorption and desorption isotherm curves (Fig. 1(f)). The isotherm curves have a similar shape, with a steep increase in adsorbed nitrogen volume in the low relative pressure region (<0.01). The initial dramatic ascent basically originates from a monolayer adsorption of nitrogen molecules on the open surface of poly-hexagonal carbon structures. Furthermore, the diagonal increase due to the relative pressure of 0.5 that follows suggests the presence of numerous fine pores with widths of a few nanometers. The nitrogen adsorption stopped growing in the relative pressure

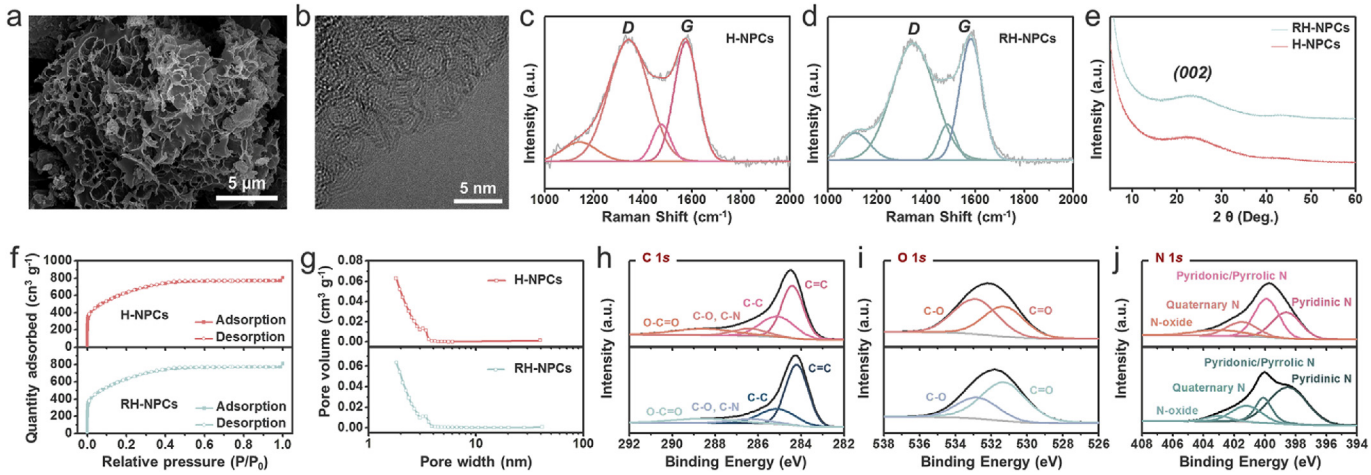

Fig. 1. (a) FE-SEM and (b) high-resolution FE-TEM images of H–NPCs. Deconvoluted Raman spectra of (c) H–NPCs and (d) RH-NPCs, and (e) their XRD patterns. (f) Nitrogen adsorption and desorption isotherm curves and (g) pore size distribution data of H–NPCs and RH-NPCs. XPS (h) C 1s, (i) O 1s, and (j) N 1s spectra of H–NPCs and RH-NPCs.

region above 0.5, and desorption curves showed no hysteresis. These results indicate that both samples have a nanoporous structure composed of a few-nanometer-scale pores. Moreover, the large amount of adsorption corresponding to ~765 $cm^3\ g^{-1}$ reveals that they have high specific surface areas induced by the nanopores. The pore size distribution data further reveal the pore structures of both samples (Fig. 1(g)). H–NPCs have nanopores below ~4 nm, and their volume increases with decreasing pore size. Furthermore, the pore structure is slightly changed after thermal treatment.

The surface properties of H–NPCs and RH-NPCs were characterized by XPS as shown in Fig. 1(h–j). The C 1*s* spectra of both samples show several bonding configurations, including sp^2 C=C, sp^3 C–C, C–O, and C–N, and O–C=O bonding peaks (Fig. 1(h)) [22]. In addition, the oxygen functional groups are mainly composed of two groups, namely, the C–O and C=O bonding configurations (Fig. 1(i)) [23]. H–NPCs have a larger bonding peak for C–O than C=O, while RH-NPCs contain larger amounts of C=O. In the case of the nitrogen functional groups, H–NPCs consist of major pyridonic N and pyridinic N structures and minor quaternary N and N-oxide configurations, while RH-NPCs have a large pyridinic N structure and minor pyridonic N, quaternary N, and N-oxide configurations (Fig. 1(j)) [21,23]. H–NPCs have high oxygen and nitrogen contents, in which C/O and C/N ratios are 6.4 and 7.1, respectively. After thermal treatment, the C/O and C/N ratios are significantly increased to 23.1 and 50.9, respectively (Table S1). The materials properties of H–NPCs and RH-NPCs are summarized in Table S1 (Supporting Information).

The electrochemical charge storage behaviors of the H–NPCs were tested in 2 M LiOH, NaOH, and KOH dissolved in distilled water over a voltage window of 0.1 to −0.9 V vs. SHE by applying different voltage ranges at a scan rate of 10 mV s^{-1} (Fig. 2(a–c)). The CV of H–NPCs is similar all in the different alkali cation-based electrolytes, where their specific capacitances were dependent on the characterized voltage ranges. As the voltage range increases from 0.2 to 1.0 V, their specific capacitances gradually increase from 98 to 224 F g^{-1}. In contrast, the specific capacitance values characterized in 0.5 M Li_2SO_4, Na_2SO_4, and K_2SO_4 dissolved in distilled water are not changed as approximately 102 F g^{-1} in spite of the application of different voltage ranges even in the different electrolyte systems (Fig. 2(a–c)). When the charge is stored by EDL formation, the capacitance response in the given voltage range should be same, because the linear *I–V* curve is divided by voltage. However, voltage hysteresis originating from PCRs distorts the *I–V* connection, causing the voltage-dependent capacitance response. Charges can be stored by PCRs of cation charge carriers on the surface redox active sites, such as oxygen and nitrogen functional groups, but not by those of anion charge carriers. Because the open circuit voltage (OCV) of H–NPCs is ~0.08 V vs. SHE in the voltage window of 0.1 ~ −0.9 V (under alkali electrolytes), the working electrode mainly stores charge by a cation charge carrier, showing voltage-dependent charge storage behavior. In contrast, in the voltage range of 0.0–1.0 V vs. SHE (under neutral electrolyte conditions), the anion is mainly stored by EDL formation, exhibiting the similar capacitance values. One of the noteworthy results is that, when the characterized voltage range is reduced in alkali electrolytes, the obtained specific capacitance values converge to the EDL capacitance value (Fig. 2(a–c)). This result suggests that the pseudocapacitance value gradually reduces with decreasing operating voltage range and finally reaches to nearly zero. Therefore, we can characterize the quantitative contribution ratio of PCRs to the overall capacitance. Fig. 2(d) shows the capacitance gap more clearly. The rest of the CV area, except the EDL capacitance characterized by the anion charge carrier, which is represented by the red-colored area of Fig. 2(d), can be calculated as the PCR contribution to the overall capacitance value. In the case of H–NPCs, a specific capacitance of about ~54.7% is attributed as PCRs (Fig. 2(d)). To further clarify this result, RH-NPCs that have much smaller heteroatom contents, but a specific surface area similar to that of H–NPCs were electrochemically tested under the same conditions. RH-NPCs showed highly reduced alkali ion storage capacitance compared with H–NPCs, while a similar anion storage capacitance was observed (Fig. 2(e)). The decrease in redox-active heteroatoms could lead to a reduction in the PCRs for RH-NPCs, while, owing to having a specific surface area similar to that of H–NPCs, EDL capacitance could not be affected. As a result, PCR contribution to the overall capacitance is greatly decreased by ~29.1% (Fig. 2(f)). The electrochemical impedance spectroscopy (EIS) measurements demonstrated that the decreased capacitance was unrelated to the changes in cell resistance after reduction, as the RH-NPCs and H–NPCs exhibited similar equivalent series resistance values (Fig. S2). This result supports the following key prerequisites: 1. Voltage dependent charge storage behaviors originate from PCRs on the redox-active heteroatoms, and 2. PCRs happen only when an alkali cation is used as a charge carrier. Therefore, experimental results make our claim that a quantitative pseudocapacitance value

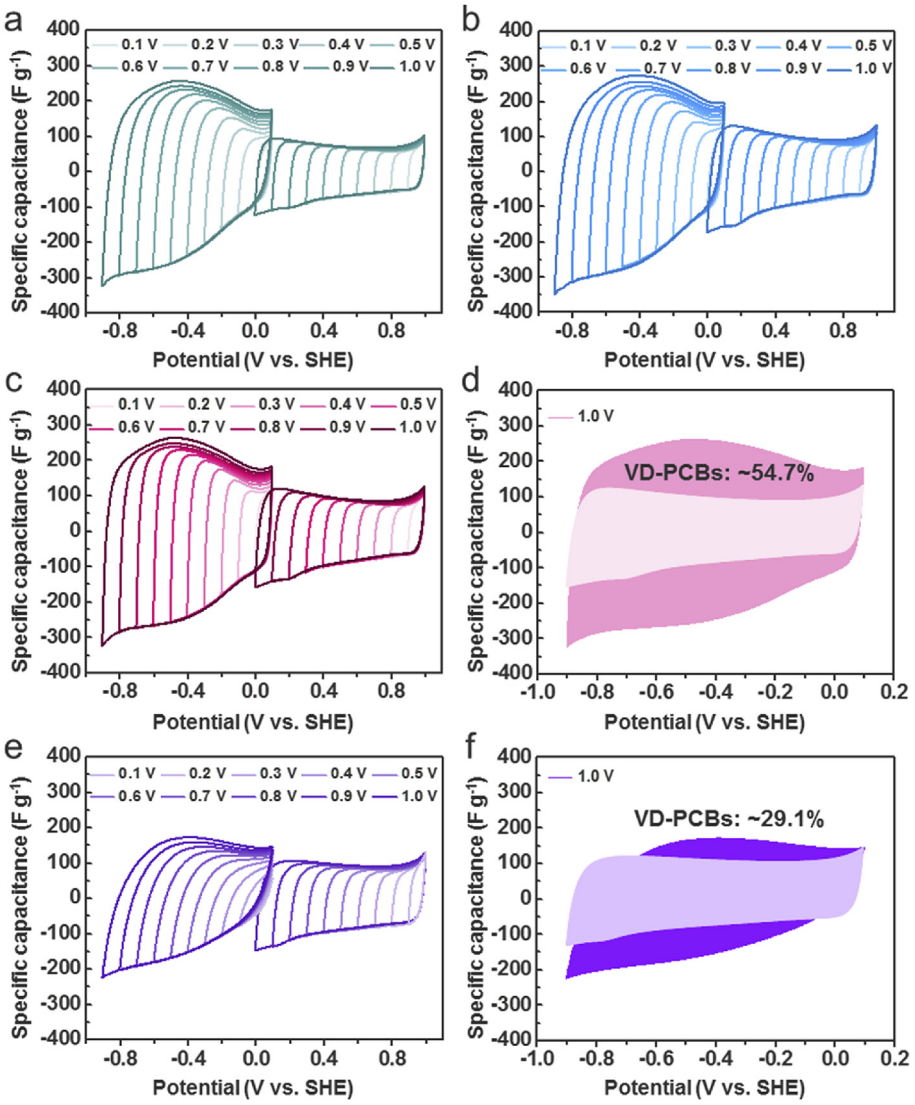

Fig. 2. CV of H–NPCs characterized in aqueous electrolytes of (a) 2 M KOH and 0.5 M K_2SO_4, (b) 2 M NaOH and 0.5 M Na_2SO_4, (c) 2 M LiOH and 0.5 M Li_2SO_4 over different voltage ranges at a scan rate of 10 mV s^{-1}. (d) Schematic expression of the CV depicted in (c): the rest area except for the overlapped area indicates VD-PCBs, which corresponds to ~54.7% of the overall capacitance. (e) CV of RH-NPCs characterized in aqueous electrolytes of 2 M LiOH and 0.5 M Li_2SO_4 over different voltage ranges at a scan rate of 10 mV s^{-1} and (f) Schematic expression for the CV depicted in (e): the rest area except for the overlapped area indicates VD-PCBs, which corresponds to ~29.1% of the overall capacitance.

can be obtained from a simple comparison of the specific capacitances in the different charge carrier-based electrolyte systems persuasive.

The voltage-dependent charge storage behaviors of H–NPCs were further observed in an organic electrolyte system based on 1 M $LiPF_6$ dissolved in ethylene carbonate (EC) and dimethyl carbonate (DMC; 1:1 *v*/*v*) (Fig. 3(a)). The specific capacitance gradually increased as the voltage window was extended incrementally from 4.5 to below 3.0 V vs. Li^+/Li. Because the OCV of H–NPCs is around 3.0 V, the lithium ion plays the role of a charge carrier in the voltage section lower than 3.0 V, leading to VD-PCBs in the extended voltage ranges. In contrast, the specific capacitance values in the voltage windows from 4.5 to 2.9, 3.1, 3.3, and 3.5 V are almost the same, despite a gradual decrease in the characterized voltage windows. This result suggests that, in the higher voltage windows, the charge storage behaviors of H–NPCs mainly occur by EDL formation. Hence, in the organic electrolyte system, we can also characterize the quantitative contribution of PCRs for H–NPCs by comparing the capacitance values characterized in the voltage ranges of 1.5–4.5 V and 3.5–4.5 V. The red colored area of Fig. 3(b) is the calculated pseudocapacitance value by subtracting the EDL capacitance value for overall capacitance value as shown in Fig. 3(a), and it corresponds to ~21.2% of the overall capacitance value. When the H–NPCs were assembled as a symmetric electrode configuration for a full cell system, the anodic and cathodic electrodes were operated in the voltage ranges of 1.5–3.0 V and 3.0–4.5 V, respectively. Furthermore, the sum of the specific capacitance values in the smaller voltage ranges was much smaller than that in the larger one (1.5–4.5 V), owing to the absence of VD-PCBs (Fig. 3(c)). The charge storage performances of H–NPCs were further characterized by using the galvanostatic charge/discharge (GCD) method at different current rates from 0.2 to 10.0 A g^{-1} in a voltage range of 1.5–4.5 V (Fig. 3(d)). The GCD profile at 0.2 A g^{-1} shows a high initial capacity of ~248 mA h g^{-1} and an average voltage of 2.8 V. In addition, the H–NPCs maintained ~60% (~148 mA h g^{-1}) of the initial capacities at 50 times higher current rates, and the initial capacity was recovered when the current rate returned to 0.2 A g^{-1} after 40 cycles (Fig. 3(d) and (e)). Moreover,

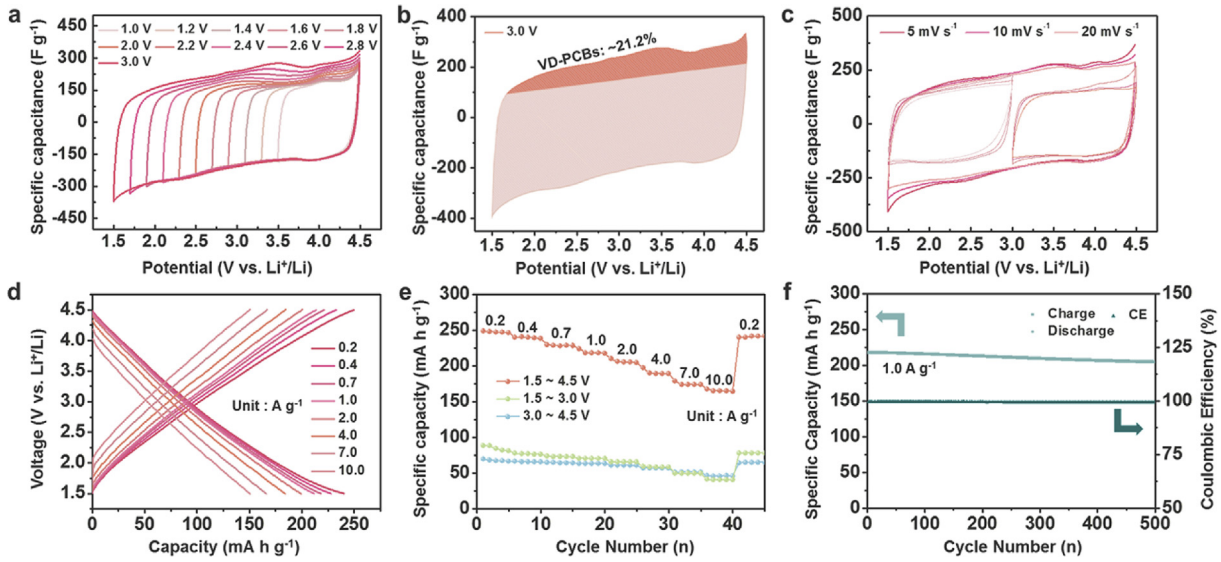

Fig. 3. Electrochemical properties of H–NPCs characterized in an electrolyte of 1 M $LiPF_6$ dissolved in an EC:DMC (1:1 v:v) solution. (a) CV over different voltage ranges at a scan rate of 10 mV s^{-1}. (b) Schematic expression of the CV depicted in (a): the rest area excluding the overlapped area indicates VD-PCBs, which corresponds to ~21.2% of the overall capacitance. (c) CV characterized in voltage windows of 1.5–3.0 V, 3.0–4.5 V, and 1.5–4.5 V vs Li^+/Li at scan rates of 5, 10, and 20 mV s^{-1}. (d) Galvanostatic charge/discharge profiles in a voltage window of 1.5–4.5 V and (e) rate capabilities characterized in voltage windows of 1.5–3.0 V, 3.0–4.5 V, and 1.5–4.5 V. (f) Cycling performance at a current rate of 1 A g^{-1} over 500 cycles.

during a repetitive charge/discharge cycling process at a constant current rate of 1 A g^{-1}, H–NPCs showed significantly stability over 500 cycles (Fig. 3(f)). The capacity retention after 500 cycles was ~93%, and the Coulombic efficiencies (CEs) were almost 100% in the entire cycling process. Meanwhile, the specific capacity values of H–NPCs operated in the voltage ranges of 1.5–3.0 V and 3.0–4.5 V

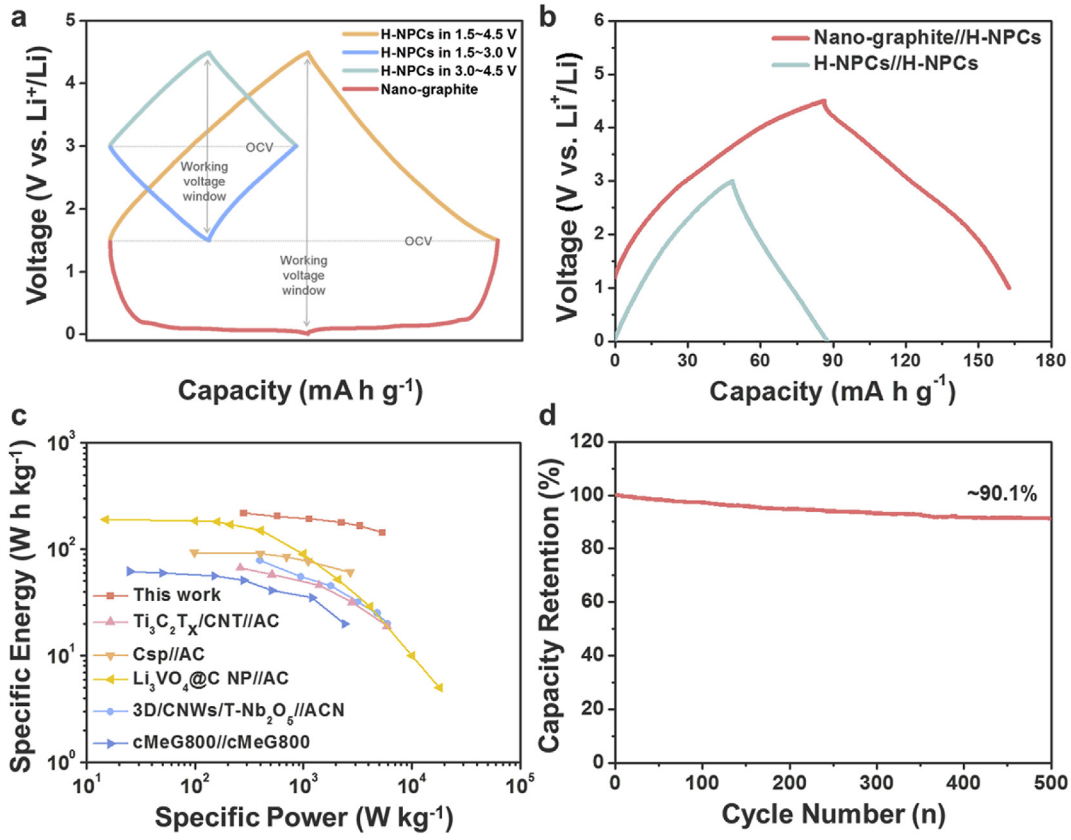

Fig. 4. (a) Schematic image for the galvanostatic charge/discharge profiles of H–NPCs and nano-graphite characterized at different voltage ranges: the nano-graphite//H–NPCs cell shows a higher energy performance than the H–NPCs//H–NPCs cells. (b) Galvanostatic charge/discharge profiles of nano-graphite//H–NPCs and H–NPCs//H–NPCs cells. (c) Ragone plots of several energy storage devices, including the nano-graphite//H–NPCs cell. (d) Cycling performance of nano-graphite//H–NPCs cell at a current rate of 1 A g^{-1} over 500 cycles.

are ~91 and 74 mA h g^{-1}, respectively (Fig. 3(e) and Fig. S3). Their sum capacity value (165 mA h g^{-1}) was much lower than the capacity value (~248 mA h g^{-1}) obtained in the voltage range of 1.5–4.5 V, coinciding with the resulting from CV. The cation and anion storage behaviors in the voltage ranges of 3.0–4.5 V and 1.5–3.0 V were maintained at ~61% (~45 mA h g^{-1}) and ~48% (~44 mA h g^{-1}), respectively, at a current rate of 10 A g^{-1} (36th cycle, (Fig. 3(e)). These results indicate that the voltage dependent pseudocapacitance is as fast and stable as the capacitive charge storage behaviors.

The schematic image shown in Fig. 4(a) depicts the charge/discharge profiles of H–NPCs working in the voltage ranges of 1.5–4.5, 1.5–3.0, and 3.0–4.5 V, and nano-graphite in a voltage range of 0.01–2.0 V, which was edited from the galvanostatic discharge/charge profile in Fig. S4. When H–NPCs were assembled with a high capacity anode material with a low voltage plateau, the energy storage devices could deliver a several times increased specific energy compared with the symmetric energy storage device (H–NPCs//H–NPCs). Fig. 4(b) represents galvanostatic charge/discharge profiles of the nano-graphite//H–NPCs and H–NPCs//H–NPCs devices at 0.2 A g^{-1}, showing the superiority of the nano-graphite//H–NPCs with an asymmetric configuration. The profile of nano-graphite//H–NPCs shows a specific capacity of 76.3 mA h g^{-1} and an average voltage of 2.88 V at 0.1 A g^{-1}, which corresponds to a specific energy and specific power of 220 Wh kg^{-1} and 288 W kg^{-1}, respectively. The detailed energy and power relationship of the nano-graphite//H–NPCs, together with previously reported results, is depicted in the Ragone plot shown in Fig. 4(c). Despite an increase in power capability by ~5400 W kg^{-1}, a high specific energy of ~143 Wh kg^{-1} is well-maintained in the nano-graphite//H–NPCs cell. The energy and power performance surpass the reference results obtained for $Ti_3C_2T_x$/CNT//AC, [24] Csp//AC, [25] Li_3VO_4@C NP//AC, [26] 3D/CNWs/T-Nb_2O_5//ACN, [27] and cMeG800//cMeG800 [28]. In addition, stable cycling was retained during 500 cycles with a capacity retention of ~90.1%. These results demonstrate the high electrochemical performances of the VD-PCBs on H–NPCs.

4. Conclusion

In summary, we prepared H–NPCs that have C/O and C/N ratios of 6.4 and 7.1, respectively, and a specific surface area of ~2290 m^2 g^{-1}. In aqueous electrolyte systems with alkali cation charge carriers, the specific capacitances of the H–NPCs showed significant changes when different voltage ranges were applied, indicating the presence of VD-PCBs. In contrast, the specific capacitance values were unchanged when an anion charge carrier was used. The results suggest that the quantitative contribution ratio of VD-PCBs can be calculated through a simple comparison of the CV obtained from the different charge carriers. The presence of VD-PCBs was also confirmed in an organic electrolyte with lithium ions as the charge carriers. With the assistance of the pseudocapacitance, H–NPCs delivered a high specific capacity of ~248 mA h g^{-1} and an average voltage of 2.8 V in a voltage window of 1.5–4.5 V In addition, H–NPCs showed high rate capabilities and stable cycling behaviors in the large operating voltage window, indicating that the VD-PCBs are significantly fast and stable. Furthermore, a full cell device based on H–NPCs delivered a significantly high specific energy of 220 Wh kg^{-1} and specific power of ~5400 W kg^{-1} with stable cycling behaviors over 500 cycles.

Acknowledgments

This research was supported by Basic Science Research Program through the National Research Foundation of Korea (NRF) funded by the Ministry of Education (NRF-2017R1C1B1004167 and NRF-2018R1A4A1025169). This study was supported by 2016 Research Grant from Kangwon National University.

Appendix A. Supplementary data

Supplementary data to this article can be found online at https://doi.org/10.1016/j.electacta.2019.02.009.

References

[1] H.D. Abruña, Y. Kiya, J.C. Henderson, Batteries and electrochemical capacitors, Phys. Today 61 (2008) 43–47.
[2] T. Brousse, D. Bélanger, J.W. Long, To be or not to be pseudocapacitive? J. Electrochem. Soc. 162 (2015) A5185–A5189.
[3] P. Simon, Y. Gogotsi, B. Dunn, Where do batteries end and supercapacitors begin? Science 343 (2014) 1210–2011.
[4] V. Augustyn, J. Come, M.A. Lowe, J.W. Kim, P.–L. Taberna, S.H. Tolbert, H.D. Abruña, P. Simon, B. Dunn, High–rate electrochemical energy storage through Li^+ intercalation pseudocapacitance, Nat. Mater. 12 (2013) 518.
[5] J. Yan, Z. Fan, T. Wei, W. Qian, M. Zhang, F. Wei, Fast and reversible surface redox reaction of graphene–MnO_2 composites as supercapacitor electrodes, Carbon 48 (2010) 3825–3833.
[6] X. Wang, S. Kajiyama, H. Iinuma, E. Hosono, S. Oro, I. Moriguchi, M. Okubo, A. Yamada, Pseudocapacitance of MXene nanosheets for high-power sodium-ion hybrid capacitors, Nat. Commun. 6 (2015) 6544.
[7] S.W. Lee, N. Yabuuchi, B.M. Gallant, S. Chen, B.–S. Kim, P.T. Hammond, Y. Shao–Horn, High–power lithium batteries from functionalized carbon–nanotube electrodes, Nat. Nanotechnol. 5 (2010) 531.
[8] S.–K. Jung, H. Kim, M.G. Cho, S.–P. Cho, B. Lee, H. Kim, Y.–U. Park, J. Hong, K.–Y. Park, G. Yoon, W.M. Seong, Y. Cho, M.H. Oh, H. Kim, H. Gwon, I. Hwang, T. Hyeon, W.–S. Yoon, K. Kang, Lithium–free transition metal monoxides for positive electrodes in lithium–ion batteries, Nat. Energy 2 (2017) 16208.
[9] H.–S. Kim, J.B. Cook, H. Lin, J.S. Ko, S.H. Tolbert, V. Ozolins, B. Dunn, Oxygen vacancies enhance pseudocapacitive charge storage properties of MoO_{3-x}, Nat. Mater. 16 (2017) 454.
[10] T. Lin, I.–W. Chen, F. Liu, C. Yang, H. Bi, F. Xu, F. Huang, Nitrogen–doped mesoporous carbon of extraordinary capacitance for electrochemical energy storage, Science 350 (2015) 1508–1513.
[11] D. Hulicova–Jurcakova, M. Kodama, S. Shiraishi, H. Hatori, Z.H. Zhu, G.Q. Lu, Nitrogen–enriched nonporous carbon electrodes with extraordinary supercapacitance, Adv. Funct. Mater. 19 (2009) 1800–1809.
[12] H. Wang, H.S. Casalongue, Y. Liang, H. Dai, $Ni(OH)_2$ nanoplates grown on graphene as advanced electrochemical pseudocapacitor materials, J. Am. Chem. Soc. 132 (2010) 7472–7477.
[13] N.R. Kim, S.M. Lee, M.W. Kim, H.J. Yoon, W.G. Hong, H.J. Kim, H.J. Choi, H.–J. Jin, Y.S. Yun, Amphicharge–storable pyropolymers containing multi-tiered nanopores, Adv. Energy Mater. 7 (2017), 1700629.
[14] Y.S. Yun, D.–H. Kim, S.J. Hong, M.H. Park, Y.W. Park, B.H. Kim, H.–J. Jin, K. Kang, Microporous carbon nanosheets with redox–active heteroatoms for pseudocapacitive charge storage, Nanoscale 7 (2015) 15051–15058.
[15] N.R. Kim, Y.S. Yun, M.Y. Song, S.J. Hong, M. Kang, C. Leal, Y.W. Park, H.–J. Jin, Citrus–peel–derived, nanoporous carbon nanosheets containing redox–active heteroatoms for sodium–ion storage, ACS Appl. Mater. Interfaces 8 (2016) 3175–3181.
[16] S.Y. Cho, H.J. Yoon, N.R. Kim, Y.S. Yun, H.–J. Jin, Sodium–ion supercapacitors based on nanoporous pyroproteins containing redox–active heteroatoms, J. Power Sources 329 (2016) 536–545.
[17] Y.S. Yun, S.Y. Cho, J. Shim, B.H. Kim, S.J. Chang, S.J. Baek, Y.S. Huh, Y. Tak, Y.W. Park, S. Park, H.–J. Jin, Microporous carbon nanoplates from regenerated silk proteins for supercapacitors, Adv. Mater. 25 (2013) 1993–1998.
[18] M. Liu, J. Niu, Z. Zhang, M. Dou, F. Wang, Potassium compound–assistant synthesis of multi–heteroatom doped ultrathin porous carbon nanosheets for high performance supercapacitors, Nano Energy 51 (2018) 366–372.
[19] J. Kopecká, D. Kopecký, M. Vrňata, P. Fitl, J. Stejskal, M. Trchová, I.P. Bober, Z. Morávková, J. prokeš, I. Sapurina, Synthesis, characterization, and electrochemistry of nanotubular polypyrrole and polypyrrole-derived carbon nanotubes, RSC Adv. 4 (2014) 14770–14784.
[20] J. Cabana, L. Monconduit, D. Larcher, M.R. Palacin, Beyond intercalation–based Li–ion batteries: the state of the art and challenges of electrode materials reacting through conversion reactions, Adv. Mater. 22 (2010) E170–E192.
[21] S.Y. Cho, Y.S. Yun, S. Lee, D. Jang, K.–Y. Park, J.K. Kim, B.H. Kim, K. Kang, D.L. Kaplan, H.–J. Jin, Carbonization of a stable β–sheet–rich silk protein into a pseudographitic pyroprotein, Nat. Commun. 6 (2015) 7145.
[22] H.J. Yoon, N.R. Kim, H.–J. Jin, Y.S. Yun, Macroporous catalytic carbon nanotemplates for sodium metal anodes, Adv. Energy Mater. 8 (2018), 1701261.
[23] M.E. Lee, H.–J. Jin, Y.S. Yun, Synergistic catalytic effects of oxygen and nitrogen functional groups on active carbon electrodes for all–vanadium redox flow batteries, RSC Adv. 7 (2017) 43227–43232.
[24] P. Yu, G. Cao, S. Yi, X. Zhang, C. Li, X. Sun, K. Wang, Y. Ma, Binder–free 2D titanium carbide (MXene)/carbon nanotube composites for

high–performance lithium-ion capacitors, Nanoscale 10 (2018) 5906–5913.
[25] B. Anothumakkool, N. Dupré, P. Moreau, D. Guyomard, T. Brousse, J. Gaubicher, Peculiar Li–storage mechanism at graphene edges in turbostratic carbon black and their application in high energy Li–ion capacitor, J. Power Sources 378 (2018) 628–635.
[26] E. Lim, W.–G. Lim, C. Jo, J. Chun, M.–H. Kim, K.C. Roh, J. Lee, Rational design of Li_3 VO_4@carbon core–shell nanoparticles as Li–ion hybrid supercapacitor anode materials, J. Mater. Chem. 5 (2017) 20969–20977.
[27] M.Y. Song, N.R. Kim, H.J. Yoon, S.Y. Cho, H.–J. Jin, Y.S. Yun, Long-lasting Nb_2O_5–based nanocomposite materials for Li–ion storage, ACS Appl. Mater. Interfaces 9 (2017) 2267–2274.
[28] R. Tjandra, W. Liu, L. Lim, A. Yu, Melamine based, n–doped carbon/reduced graphene oxide composite foam for Li-ion hybrid supercapacitors, Carbon 129 (2018) 152–158.